

# Direct Contact Jet Impingement Cooling with Non-conductive Fluid for Power Converters that Enables Increased Power Density

Matthew Jahnes  
Columbia University  
matthew.jahnes@columbia.edu

Michael Owen  
Tau Motors, Inc.  
mike@taumotors.com

W. Wesley Pennington  
Tau Motors, Inc.  
wesley@taumotors.com

Matthias Preindl  
Columbia University  
matthias.preindl@columbia.edu

**Abstract**—This digest presents a jet impingement cooling scheme that is adapted to an existing air-cooled power converter. This jet impingement cooling is novel as it leverages automatic transmission fluid (ATF), a non-electrically conductive fluid, as the liquid medium. This allows for direct contact of the liquid medium with conductive components, including the exposed heat dissipating pad of a FET which is commonly connected to its drain and held at high potential. This is in contrast with typical jet-impingement cooling schemes which use ethylene-glycol to cool a heatsink that is then interfaced with the heat dissipating components. The proposed scheme negates the need for this heatsink and the electrically insulating and thermally conductive interface between it and the FETs. The resulting cooling technique allows for a more efficient heat transfer into the liquid medium. Results are validated with simulation. Through comparison with an existing high-performance forced-air cooler it is demonstrated that this cooling method will allow for both an increase in output power and a decrease in volume, resulting in a >50% increase in power density. Lastly, the efficacy of this scheme in a motor drive environment is presented, where it is shown that this cooling method alongside an LC filter placed between the inverter and the motor will result in both increased efficiency and power density.

## I. INTRODUCTION

High density power conversion cannot be achieved through exclusively electrical design. Inverter efficiencies are approaching and in some cases exceeding 99% due to improvements in electrical design [1]–[3] allowing for an associated decrease in waste heat that needs to be dissipated. However, as overall power levels increase, any non-perfect efficiency will necessitate some manner of heatsink, and heatsink inclusion will drive down both the volumetric and gravimetric power density.

Power density is of increasing importance as integrated power electronics become more prevalent in vehicles. This includes on board chargers and motor inverters for EVs [4] and aerospace applications [5], [6]. These areas are especially concerned with the gravimetric power density as heavier vehicles will exhibit decreased performance. This suggests that heatsink design and how thermal solutions integrate with their associated power electronics will become more important as more vehicles become electrified.

There are typical approaches to cooling for power electronics that have been used in both industry and academia. Passive conduction of waste heat into the air can suffice for low power

applications. Higher power applications will utilize a separate heatsink, thermally connected to the heat sources, with either forced air or liquid used to remove heat from the heatsink. Forced air cooling is straightforward as there are many off-the-shelf solutions that can be adapted for different applications. Liquid cooling is typically higher performing but comes at the cost of increased complexity, requiring a water block, pump, radiator, and associated tubing.

This increased complexity can be worth it, as can be seen in Fig. 1. High powers can be achieved with air cooling, but high power densities are almost exclusively achieved with liquid cooling. This is because the liquids typically used in liquid cooling systems (water, ethylene glycol) have higher thermal conductivity, resulting in more efficient transfer of heat into the medium that dissipates it.

Fig. 1 references a proposed power converter with two different types of heat removal systems. One cooling solution utilizes an off-the-shelf (OTS) forced-air server CPU heatsink. The second system is in regards to the topic of this digest, which presents a novel cooling solution in which the sources of heat within a power converter are cooled via a direct contact jet impingement cooling technique. This differs from existing jet impingement cooling literature as the proposed solution uses a non-conductive automotive transmission fluid (ATF) as the liquid medium. The ATF circulates around the components and cools them through direct contact without the need for any interface between the liquid medium and heat source. Other solutions [7]–[9] use jet impingement cooling within a heatsink that then makes contact with the components.

The proposed technique removes the need for both a bulky heatsink as well as any associated thermal interface pad between the heat source and the heatsink as the ATF makes direct contact with anything it is intended to cool. Furthermore, in many automotive applications, ATF and its associated pumping and cooling infrastructure is already present, and there is little additional overhead associated with using it as a power electronics coolant. The efficacy of the proposed ATF direct contact jet impingement cooling method for power electronics is shown through high-fidelity simulation. Lastly, it is shown that this cooling scheme in conjunction with an LC filter can provide both increased power density and efficiency in a motor drive environment when compared to typical motor drives.

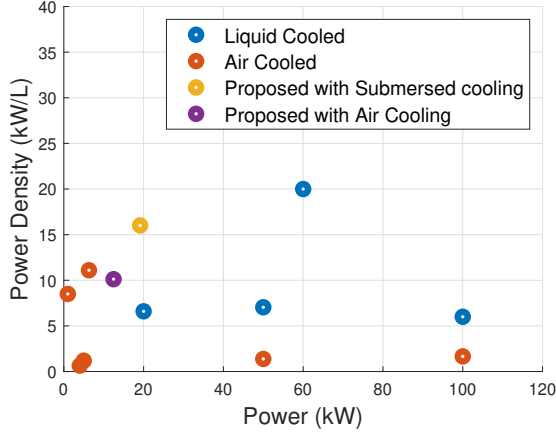


Fig. 1. Performance of liquid vs. air cooled converters [10]–[18].

## II. LOSS CALCULATION

The proposed converter used in this experimental heatsink setup is a 3-phase inverter with a schematic that can be seen in Fig. 2. This inverter has a novel addition to the typical 3-phase half bridge in the form of an additional capacitor  $C_A$ . This capacitor is intended to reduce the voltage ripple on both the DC bus and grid connection simultaneously, but as this is a thermal management paper the exact functionality of  $C_A$  is beyond the scope.

There are two main sources of loss in this inverter, FET losses and inductor losses. FET losses can be split into two components, switching loss and conduction loss. Similarly, inductor losses can be split into a resistive loss within the winding and a hysteresis loss within the core.

1) *FET Losses*: Rigorous quantification of FET losses must consider the instantaneous operating point of the converter. The output is a sine wave, and as such output voltage  $V_{out}$ , output current  $I_{out}$ , and duty cycle  $D$  are dynamic and are written as

$$V_{out}(\theta) = \frac{V_{DC}}{2} + \sqrt{2}V_{out,RMS} \sin(\theta) \quad (1)$$

$$I_{out}(\theta) = \sqrt{2}I_{out,RMS} \sin(\theta - \phi) \quad (2)$$

$$D(\theta) = \frac{V_{out}(\theta)}{V_{DC}}. \quad (3)$$

where  $\theta$  is the instantaneous phase of the output sine wave voltage and  $\phi$  is the phase difference between the output current and the output voltage. The peak to peak inductor ripple current  $I_{L,p-p}$  is calculated with

$$I_{L,p-p}(\theta) = \frac{D(\theta)(1-D(\theta))V_{DC}}{f_{sw}(\theta)L_{sw}}. \quad (4)$$

The conduction losses are found considering  $I_{L,p-p}(\theta)$  and are calculated with

$$P_{cond}(\theta) = R_{on} \left( I_{out}(\theta)^2 + \left( \frac{1}{2\sqrt{3}} I_{L,p-p}(\theta) \right)^2 \right) \quad (5)$$

where  $R_{on}$  is the datasheet specified on resistance of the FET and  $\frac{1}{2\sqrt{3}} I_{L,p-p}^2$  is the RMS value of the inductor current ripple component.

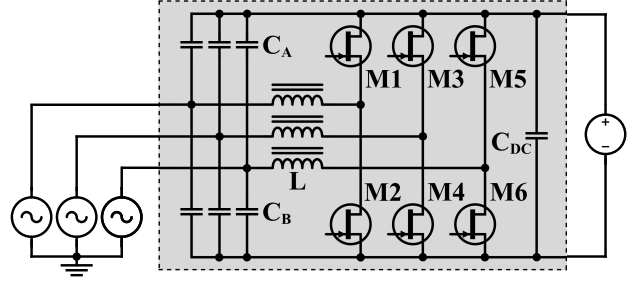


Fig. 2. Circuit topology of the inverter used for heatsink testing.

The process for calculating the switching losses used in this paper relies heavily upon a quantification of switching energy as a function of drain current  $I_d$ , gate resistance  $R_g$ , and FET drain-source voltage  $V_{ds}$ . The datasheet of the SiC FETs used in this converter provides these values which allows for the mapping of switching energies  $E_{on}(I_d, R_g, V_{ds})$  and  $E_{off}(I_d, R_g, V_{ds})$  to be formulated.  $R_g$  and  $V_{ds}$  can be considered static values and are not included in the following theory.

As previously mentioned, the output current and voltage of a single phase can be considered dynamic and therefore the distinction between hard and soft switching over one cycle of the grid must be considered. Analytically, this distinction can be made with

$$E_{sw}(\theta) = \begin{cases} E_{off}(I_a(\theta)) + E_{off}(I_b(\theta)) & I_a(\theta) > 0, I_b(\theta) < 0 \\ E_{on}(I_a(\theta)) + E_{off}(I_b(\theta)) & I_a(\theta), I_b(\theta) < 0 \\ E_{off}(I_a(\theta)) + E_{on}(I_b(\theta)) & I_a(\theta), I_b(\theta) > 0 \end{cases} \quad (6a)$$

$$I_a(\theta) = I_{DC} - \frac{I_{L,p-p}(\theta)}{2} \quad (6b)$$

$$I_b(\theta) = I_{DC} + \frac{I_{L,p-p}(\theta)}{2} \quad (6c)$$

where  $I_a$  and  $I_b$  are the peak and valley inductor current values, respectively. Visually, the hard and soft switching distinction can be seen in Fig. 3. This distinction is important to make as turn-on energies can be significantly greater than the turn-off energies.

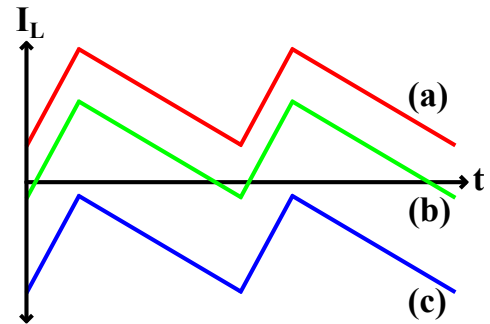


Fig. 3. Three different  $I_L$  cases used in calculating FET switching loss per cycle. a) turn-on loss at peak, turn-off loss at valley, b) turn-off loss at peak, turn-off loss at valley c) turn-on loss at peak, turn-off loss at valley.

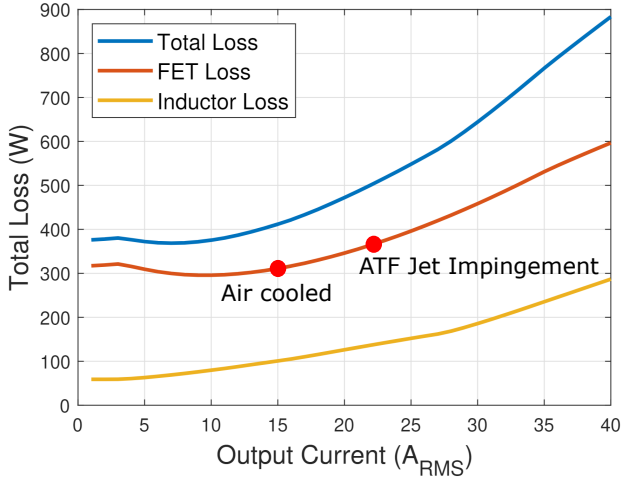


Fig. 4. Loss of the inverter as a function of output current, split between inductor and FET losses. Red dots indicate maximum values for their respective cooling schemes.

The switching loss  $P_{sw}$  can then be found with

$$P_{sw}(\theta) = f_{sw} E_{sw}(\theta). \quad (7)$$

Finally, the total FET loss  $P_{FET}$  over one cycle of the grid can be found by averaging the sum of both FET loss mechanisms from  $0 < \theta < 2\pi$

$$P_{FET} = \frac{1}{2\pi} \int_0^{2\pi} (P_{cond}(\theta) + P_{sw}(\theta)) d\theta. \quad (8)$$

2) *Inductor Losses*: Inductor losses are calculated by splitting the total loss into two components, core loss and copper (winding) loss. Copper loss is calculated with

$$P_{Cu}(\theta) = R_{DC} I_{out}(\theta)^2 + R_{PWM}(\theta) \left( \frac{1}{2\sqrt{3}} I_{L,p-p}(\theta) \right)^2, \quad (9)$$

where  $R_{DC}$  is the DC winding resistance and  $R_{PWM}(\theta)$  is the frequency dependant winding resistance of the inductor. As the fundamental frequency within the inductor is the switching frequency, and the switching frequency will change over one cycle of the grid,  $R_{PWM}(\theta)$  is dynamic. The frequency dependant component of the winding resistance is an intrinsic value of the chosen winding wire gauge and type. The core loss of the inductor is calculated with

$$\begin{aligned} P_{core}(\theta) &= k f_{sw}(\theta)^a B_{pk}(\theta)^b \\ &= k f_{sw}(\theta)^a \left( \frac{4\pi N I_{pk}(\theta) 10^{-2}}{l_g + (l_m/\mu_r)} \right)^b, \end{aligned} \quad (10)$$

where  $k, a, b$  are coefficients of the core, typically supplied by its manufacturer.  $B_{pk}(\theta)$  and  $I_{pk}(\theta)$  are the peak flux and current densities, respectively, and are dynamic.  $N, l_g, l_m$ , and  $\mu_r$  are the turn number, air-gap, and length of the magnetic path and permeability, respectively, and are static values of the inductor.

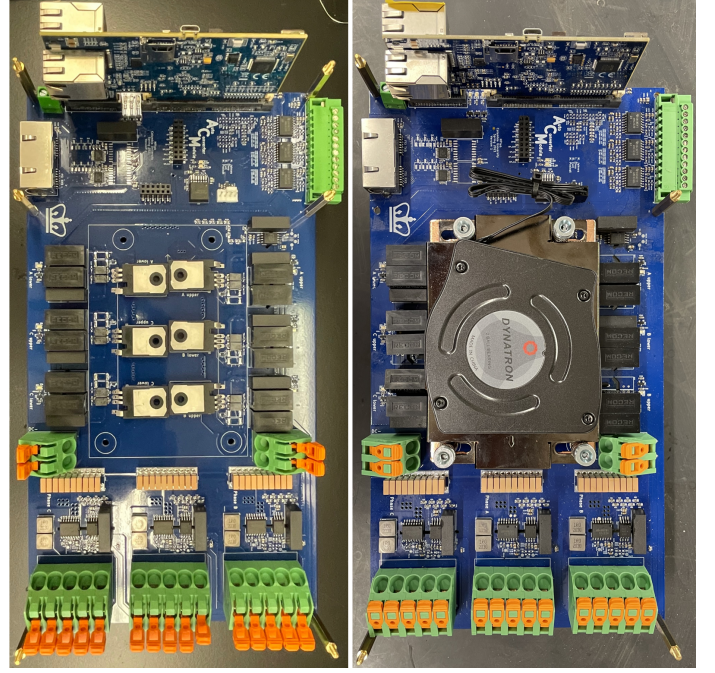


Fig. 5. Converter without heatsink (left) and converter with heatsink (right).

In a similar manner to calculating the FET loss, the average inductor losses are found by taking the average of the losses over one cycle of the grid according to

$$P_{Inductor} = \frac{1}{2\pi} \int_0^{2\pi} (P_{core}(\theta) + P_{Cu}(\theta)) d\theta. \quad (11)$$

Lastly, the total loss is simply

$$P_{total} = P_{FET} + P_{Inductor}. \quad (12)$$

The converter used in this experiment is designed to interface with a 277V<sub>LL</sub> grid and maintain a 900V DC Bus. The value of the inductance  $L$  is 4.5  $\mu$ H. This converter uses a variable-frequency critical soft-switching (VFCSS) scheme. This switching scheme allows for the converter to operate in the zero-voltage switching region (waveform (b) in Fig. 3) over a variety of loads, as described in [19]–[21]. The VFCSS switching frequency range for this converter is from 50kHz to 1.16MHz. The FETs are CREE C3M0032120k 3rd generation SiC FETs.

The total loss of all three phases of the inverter as RMS output current is swept from 0 to 40A can be seen in Fig. 4. 40A represents a reasonable maximum current for this FET while it is operating near its maximum junction temperature in accordance with its datasheet.

### III. MAXIMUM POWER USING AIR COOLING

The OTS heatsink used for the air cooling results is a Dynatron A31, a CPU server forced-air heatsink. This was chosen for its large flat surface that is conducive towards mounting multiple FETs underneath it. The OTS forced-air heatsink as well as the FETs can be seen in Fig. 5. All six

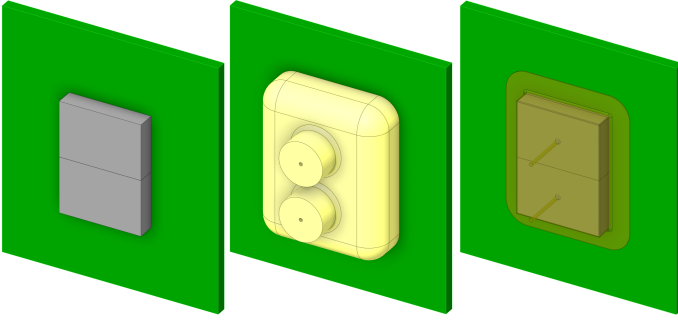


Fig. 6. Two neighboring FETs (left), jet impingement cooling jacket (center), and coolant flow volume (right).

FETs are cooled with the same heatsink, and the volume of the converter is 1.46L (1.232L of this is PCB and component volume and 0.228L is attributed to the volume of all three external inductors).

The maximum dissipation can be calculated in a straightforward manner given the thermal resistance of all the components. The electrical equivalent of the thermal circuits can be seen in Fig. 7, where  $R_A$  and  $R_B$  represent the thermal resistances of the thermal pad and heatsink, respectively, for the OTS forced-air heatsink scheme. For the liquid cooled case,  $R_A$  and  $R_B$  represent the thermal resistances of the FET case to liquid and the liquid to air, respectively. The thermal resistance between the FET junction and case  $R_{\theta JC}$  is  $0.45^\circ\text{C}/\text{W}$ .

The OTS forced-air heatsink scheme has all six FETs sharing a common heatsink with the thermal pad  $R_{\theta P}$  as  $0.25^\circ\text{C}/\text{W}$  and the heatsink  $R_{\theta H}$  as  $0.173^\circ\text{C}/\text{W}$ . As all six FETs share a heatsink, the heat effectively travels through the parallel combination of the six FETs and thermal pads in series with the heatsink, resulting in the following:

$$P_{diss} = \frac{T_{J,max} - T_a}{\frac{1}{6}(R_{\theta JC} + R_{\theta P}) + R_{\theta H}}. \quad (13)$$

For a maximum allowable FET junction temperature  $T_{J,max}$  of  $150^\circ\text{C}$  and an ambient air temperature  $T_a$  of  $60^\circ\text{C}$ , the maximum tolerable total FET loss is 310W, roughly 50W per FET for the OTS forced-air heatsink scheme. Fig. 4 shows that with this forced-air heatsink, the maximum allowable output current of this inverter is 15A per phase, well below the capabilities of the FET, which represents 12.47kW in total and a power density of 8.54kW/L. This result implies that the limit on maximum power for this converter lies within the OTS forced-air heatsink and improving this will result in increased power density and output power.

#### IV. MAXIMUM POWER USING DIRECT CONTACT JET IMPINGEMENT COOLING

The previous section showed that the heat dissipation limits of OTS forced-air heatsink define the maximum power output of this converter. This section shows, through computational fluid dynamic (CFD) simulation, that with direct contact jet impingement cooling, the limiting factor for power output can

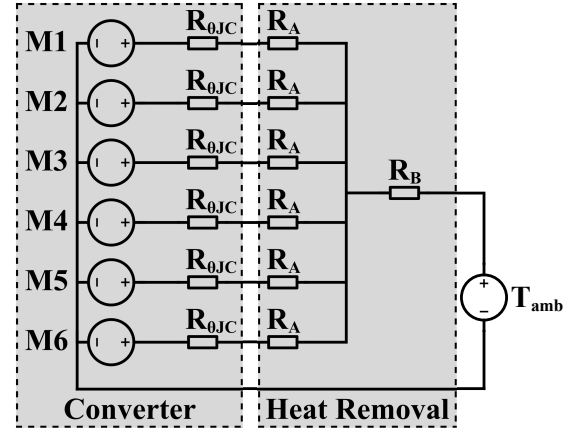


Fig. 7. Thermal path equivalent electrical circuit.

be improved, resulting in increased output power. Furthermore, the volume can be reduced, resulting in a compound increase in power density.

Automatic Transmission Fluid (ATF) is used as the liquid coolant; ATF is non-conducting, allowing direct contact between the exposed pad of the FET and the coolant. Furthermore, in many automotive applications, ATF and its associated pumping and cooling apparatuses are already in place.

Each FET is jacketed with a tight clearance to the upper (heat rejecting) surface while pressurized ATF is injected through a small port. The tight clearance maintains a high bulk velocity relative to the FET, yielding high heat transfer coefficients. The peak heat transfer coefficient occurs around the jet impingement point, which may be placed directly over the junction within the FET. The tight clearance also reduces coolant residence time and temperature for a given flow rate, while back pressure is maintained such that the heat dissipating surface of the FET remains fully wetted. Maintaining a low coolant temperature is beneficial for both cooling the FET and protecting the coolant itself from thermal degradation.

Fig. 6 shows a jet impingement cooling jacket for a pair of neighboring FETs. For convenience, the FET leads are neglected and it is assumed that there is no space between the FETs and the PCB. The ATF flows through the jet impingement port, along the surface of the FET, and exits at the perimeter of the jacket to be sumped and returned. This has the added benefit of also cooling the area of the PCB local to the FET, although we have neglected this effect in the model.

CFD modeling was performed with ANSYS CFX with temperature dependent density, viscosity, and thermal conductivity applied to the ATF. The datasheet-specified value for junction-to-case thermal resistance  $R_{\theta JC} = 0.45^\circ\text{C}/\text{W}$  was used to calculate an effective bulk thermal conductivity for the FET bodies such that the temperature difference developed across each FET at 60W each is  $27^\circ\text{C}$ , with the heat load applied at the base of the FET body; hence the temperature that develops there is the junction temperature. We disallow thermal contact between the bottom of the FET and the board, as well as between the perimeter of the FET and the coolant so that

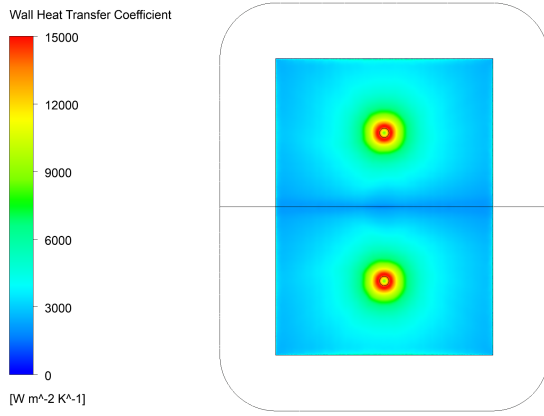


Fig. 8. Heat transfer coefficient.

all heat must be rejected from the upper surface by liquid cooling. The inlet coolant temperature is assumed to be  $75^{\circ}\text{C}$ , a reasonable value for automotive applications.

The jacket clearance and injection port diameter were varied to determine values that are capable of rejecting 60W per FET in steady state for a reasonable oil flow, defined as less than 4 LPM for the entirety of the six FETs, and for a reasonable total pressure, defined as less than 20psi. The maximum allowable junction temperature is assumed to be  $150^{\circ}\text{C}$ , and the maximum allowable ATF temperature is assumed to be  $115^{\circ}\text{C}$ . In light of these requirements, values of the jacket clearance and injection port ID of 0.25mm and 1mm, respectively, were selected. As can be seen in Fig. 9, this results in a minimum flow rate required to keep the junction temperature below  $150^{\circ}\text{C}$  of only 2.5LPM (total for all 6 FETs), but a minimum flow rate of 3.7LPM, or 0.63LPM/FET, is required to keep the maximum coolant temperature below  $115^{\circ}\text{C}$ .

The mass-flow averaged coolant temperature rise at the outlet for this flow rate is then  $3.3^{\circ}\text{C}$ , while the total heat required at the inlet is 12.9PSI. The average heat transfer coefficient over the FET is  $\approx 3900\text{Wm}^{-2}\text{K}^{-1}$ , weighted toward the region of jet impingement. These results demonstrate that the direct contact ATF jet impingement cooling scheme can achieve 19.13kW operation. The volume is reduced to 1.195L through removal of the OTS forced-air heatsink (inductor volume is retained) which results in a power density improvement of 87.47%, from 8.54kW/L to 16.01kW/L.

## V. MOTOR DRIVE CONFIGURATION RESULTS

Using ATF as the liquid heat conductive medium is convenient for when this inverter is configured as a motor drive.

TABLE I  
MOTOR DRIVE PERFORMANCE COMPARISON

Configuration	Power (kW)	Volume (L)	Efficiency	Density (kW/L)
Air, without LC	12.47	1.232	85.52%	10.12
Air, with LC	12.47	1.460	87.35%	8.54
Liquid, without LC	19.13	0.967	86.13%	19.78
Liquid, with LC	19.13	1.195	90.04%	16.01

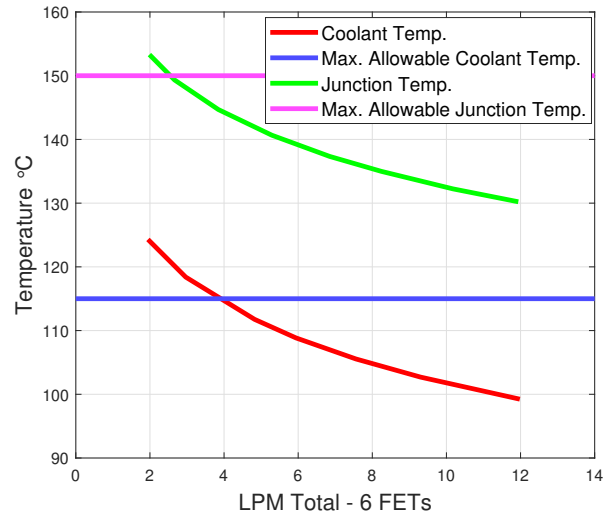


Fig. 9. Coolant and junction temperatures vs. flow rate.

ATF is commonly used to cool traction motors and with the proposed technology the cooling system between the motor and the power electronics can be shared. Therefore it is advantageous to examine the efficacy of this solution on the context of a motor drive configuration.

The cooling solution proposed in this paper can be used in conjunction with the already established work described in [4]. The important aspect of this previously established work that relates to the proposed is the addition of the output LC filter to the typical motor drive configuration. This LC filter is present in grid-tied inverters of this topology (which can be seen in Fig. 2) but not in typical motor inverters. This LC filter allows the motor to be driven by a near sinusoidal source, as opposed to the PWM source of typical motor drivers.

This technique reduces the core losses of the motor resulting in improved efficiency. The motor used in [4] has an efficiency of 88% and 92% when driven by PWM and sine wave sources, respectively. The addition of the LC filter results in increased volume, equal to the volume of the LC filter itself, which presents a design tradeoff between efficiency and volume. However, this additional volume can be offset by the volume decrease associated with the proposed jet impingement cooling scheme.

Table I is created considering the same motor efficiencies under different motor inverter types found in [4]. It considers all possible combinations of air and liquid cooling with and without LC filtering. Losses are calculated using the methods in Section II. Motor efficiencies under different drive types are of those found in [4]. It can be seen in Table I that the volume reduction allowed by the proposed jet impingement cooling scheme is greater than the volume increase of the additional LC filter. Furthermore, the increased output power allowed by the improved cooling allows for a 58.2% increase in power density from 10.12 kW/L to 16.01kW/L from a typical motor drive with air cooling and no additional LC filter.

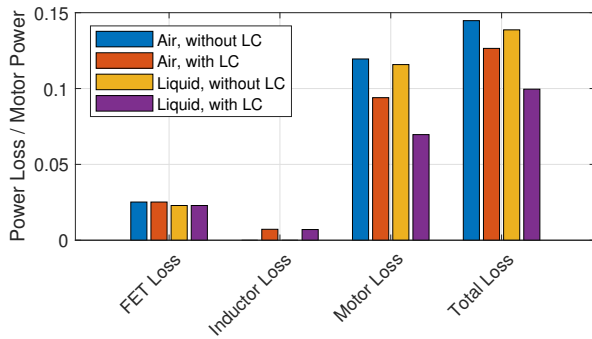


Fig. 10. Loss breakdowns of the four motor drive configurations.

Lastly, Fig. 10 shows the distribution of losses for each of the four configurations in Table I. It can be seen that the losses incurred in the LC filter are outweighed by the losses saved in the motor.

## VI. CONCLUSION

The results presented in this paper demonstrate that moving from a high-performance OTS forced-air cooling scheme to the proposed direct contact ATF jet impingement technique allows for an increase in power output from 12.47kW to 19.13kW. This also allows for a decrease in volume from 1.46L to 1.195L, which results in a corresponding increase in power density by 58% from 10.12kW/L to 16.01kW/L when used in a grid-tied inverter application. The increase in power density as a motor drive is 58.2% from 10.12kW/L to 16.01kW/L with a corresponding increase in efficiency from 85.52% to 90.04%. The maximum output current is still limited by the waste heat rejection scheme but is now much closer to the maximum rated current of the FETs, resulting in a more balanced design.

Further work regarding this research includes constructing the physical jet impingement cooling apparatus and validating the simulated results. Designing a new PCB with layout optimized for use with this proposed technology which can potentially result in further improvements on power density.

## REFERENCES

- [1] Yanjun Shi, Lu Wang, Ren Xie, and Hui Li. Design and implementation of a 100 kw sic filter-less pv inverter with 5 kw/kg power density and 99.2% cec efficiency. In *2018 IEEE Applied Power Electronics Conference and Exposition (APEC)*, pages 393–398, 2018.
- [2] Satoshi Nakazaki, Shogo Ito, Hidemine Obara, and Atsuo Kawamura. Discussion on loss breakdown of 99.6% efficiency two battery heecs inverter. In *2019 21st European Conference on Power Electronics and Applications (EPE '19 ECCE Europe)*, pages P.1–P.9, 2019.
- [3] J. Azurza Anderson, E. J. Hanak, L. Schrittwieser, J. W. Kolar, and G. Deboy. Towards a 99.5% efficient all-silicon three-phase seven-level hybrid active neutral point clamped inverter. In *2018 IEEE International Power Electronics and Application Conference and Exposition (PEAC)*, pages 1–7, 2018.
- [4] Michael Eull, Liwei Zhou, Matthew Jahnes, and Matthias Preindl. Bidirectional non-isolated fast charger integrated in the electric vehicle traction drivetrain. *IEEE Transactions on Transportation Electrification*, pages 1–1, 2021.
- [5] R. De Maglie, G. Osvald, J. Engstler, A. Engler, and J.-P. Carayon. Optimized 70kw power inverter dedicated to future aircraft applications. In *2009 13th European Conference on Power Electronics and Applications*, pages 1–10, 2009.

- [6] U. Nasir, S. Chowdhury, A. La Rocca, Y. Chen, P. Wheeler, C. Gerada, S. Bozhko, and T. Yang. A sic based 2-level power converter for shape-and-space-restricted aerospace applications. In *2019 IEEE 13th International Conference on Power Electronics and Drive Systems (PEDS)*, pages 1–7, 2019.
- [7] Kyle Gould, Steve Q. Cai, Charles Neft, and Avijit Bhunia. Liquid jet impingement cooling of a silicon carbide power conversion module for vehicle applications. *IEEE Transactions on Power Electronics*, 30(6):2975–2984, 2015.
- [8] Scot K. Wayne, Sreekanth Narumanchi, Mark Mihalic, Gilbert Moreno, Kevin Bennion, and Jana Jeffers. Advanced liquid cooling for a traction drive inverter using jet impingement and microfinned enhanced surfaces. In *Fourteenth Intersociety Conference on Thermal and Thermomechanical Phenomena in Electronic Systems (ITherm)*, pages 1064–1073, 2014.
- [9] Bassem Mouawad, Robert Skuriat, Jianfeng Li, C. Mark Johnson, and Christina DiMarino. Development of a highly integrated 10 kv sic mosfet power module with a direct jet impingement cooling system. In *2018 IEEE 30th International Symposium on Power Semiconductor Devices and ICs (ISPSD)*, pages 256–259, 2018.
- [10] Byeong-Mun Song, Moon-Ho Kye, and Rae-Young Kim. Design of a cost-effective dc-dc converter with high power density for magnetron power supplies. In *The 2010 International Power Electronics Conference - ECCE ASIA -*, pages 137–141, 2010.
- [11] Juyoung Sim, Junyoung Lee, Hyunjun Choi, and Jee-Hoon Jung. High power density bidirectional three-port dc-dc converter for battery applications in dc microgrids. In *2019 10th International Conference on Power Electronics and ECCE Asia (ICPE 2019 - ECCE Asia)*, pages 843–848, 2019.
- [12] Md Rishad Ahmed and Yun Li. A low-cost, high-power-density dc-dc converter for hybrid and electric vehicle applications. In *2019 21st European Conference on Power Electronics and Applications (EPE '19 ECCE Europe)*, pages P.1–P.8, 2019.
- [13] Y. Li, Y. Zhang, X. Yuan, L. Zhang, Z. Song, M. Wu, F. Ye, Z. Li, Y. Li, Y. Xu, and Z. Wang. 500 kw forced air-cooled silicon carbide (sic) three-phase dc/ac converter with a power density of 1.246 mw/m<sup>3</sup> and efficiency gt:98.5%. *IEEE Transactions on Industry Applications*, 57(5):5013–5027, 2021.
- [14] Lei Zhang, Yan Li, Yonglei Zhang, Xibo Yuan, Zijian Wang, and Zhe Li. A 100kw forced-air-cooled sic mosfet converter achieving a power density of 1.657kw/l and an efficiency over 98.5%. In *2020 IEEE 9th International Power Electronics and Motion Control Conference (IPEMC2020-ECCE Asia)*, pages 3443–3448, 2020.
- [15] Bret Whitaker, Adam Barkley, Zach Cole, Brandon Passmore, Ty McNutt, and Alexander B. Lostetter. High-frequency ac-dc conversion with a silicon carbide power module to achieve high-efficiency and greatly improved power density. In *2013 4th IEEE International Symposium on Power Electronics for Distributed Generation Systems (PEDG)*, pages 1–5, 2013.
- [16] G. Calderon-Lopez and A. J. Forsyth. High power density dc-dc converter with sic mosfets for electric vehicles. In *7th IET International Conference on Power Electronics, Machines and Drives (PEMD 2014)*, pages 1–6, 2014.
- [17] Yanjun Shi, Yuxiang Shi, Lu Wang, Ren Xie, and Hui Li. A 50kw high power density paralleled-five-level pv converter based on sic t-type mosfet modules. In *2016 IEEE Energy Conversion Congress and Exposition (ECCE)*, pages 1–8, 2016.
- [18] Ning He, Min Chen, Junxiong Wu, Nan Zhu, and Dehong Xu. 20-kw zero-voltage-switching sic-mosfet grid inverter with 300 khz switching frequency. *IEEE Transactions on Power Electronics*, 34(6):5175–5190, 2019.
- [19] Liwei Zhou and Matthias Preindl. Optimal-frequency critical soft switching method of synchronous dc/dc converter based on model predictive control. In *2019 IEEE Applied Power Electronics Conference and Exposition (APEC)*, pages 2989–2994, 2019.
- [20] Bharat Agrawal, Liwei Zhou, Ali Emadi, and Matthias Preindl. Variable-frequency critical soft-switching of wide-bandgap devices for efficient high-frequency nonisolated dc-dc converters. *IEEE Transactions on Vehicular Technology*, 69(6):6094–6106, 2020.
- [21] Liwei Zhou and Matthias Preindl. Variable-switching constant-sampling frequency critical soft switching mpc for dc/dc converters. *IEEE Transactions on Energy Conversion*, 36(2):1548–1561, 2021.